Research Article | Vol. 28, No. 21 / 12 October 2020 / Optics Express 31594
Optics EXPRESS

Sensing refractive index gradients along dielectric nanopillar metasurfaces

XIAOYUAN LU,[1,5] VINI GAUTAM,[2] DMITRY SHISHMAREV,[3] AND VINCENT R. DARIA[3,4,6]

[1]School of Medical Engineering, Xinxiang Medical University, Xinxiang 453003, China
[2]Department of Biomedical Engineering, University of Melbourne, Victoria 3010, Australia
[3]John Curtin School of Medical Research, Australian National University, ACT 2601, Australia
[4]Research School of Physics, Australian National University, ACT 2601, Australia
[5]luxy@xxmu.edu.cn
[6]vincent.daria@anu.edu.au

Abstract: Metasurfaces exhibit unique optical properties that depend on the ratio of their refractive index and that of their surroundings. As such, they are effective for sensing global changes in refractive index based on the shifts of resonances in their reflectivity spectra. However, when used as a biosensor, the metasurface can be exposed to a spatial distribution of biomolecules that brings about gradients in refractive index along the plane of the metasurface. Such gradients produce complex global reflectivity spectrum but with distinct optical enhancements in localized areas along the metasurface. Here, we propose a unique sensing paradigm that images and maps out the optical enhancements that are correlated with the spatial distribution of the refractive index. Moreover, we designed a metasurface whose resonances can be tuned to detect a range of refractive indices. Our metasurface consists of silicon nanopillars with a cylindrical nanotrench at their centers and a metal plane at the base. To assess its feasibility, we performed numerical simulations to show that the design effectively produces the desired reflectivity spectrum with resonances in the near-infrared. Using an incident light tuned to one of its resonances, our simulations further show that the field enhancements are correlated with the spatial mapping of the gradients of refractive indices along the metasurface.

1. Introduction

Metasurfaces are planar nanostructured sheets that produce enhanced electromagnetic field hotspots making them useful for a range of applications from biosensors [1–5], energy harvesters [6] to thermal emitters [7]. The field enhancements in metasurfaces are highly dependent on the ratio of the material's refractive index and that of its surroundings. These properties have been applied mostly in biosensing, where changes in the reflectivity spectra or shifts in the resonant wavelength are exploited for sensing the refractive index of the surrounding medium [2,3,8,9]. However, in complex sensing conditions, such as using the metasurface as an artificial niche for cell studies [10], spatial gradients in refractive indices arise due to arbitrary distributions of biomolecules. Such gradients in refractive indices can yield spatially localized optical enhancements that can be used to map the refractive index distributions along the metasurface. Sensing and mapping the spatial distribution of refractive indices can provide novel insights especially when using the metasurface as lab-on-a-chip sensors for assessing biochemical, bacteria or virus distributions.

Metasurfaces have been used to identify biochemicals and molecules via refractometric sensing using plasmonic nanostructures [9,11–14]. Dielectric metasurfaces [15] have been integrated into functional biosensor chips [16] and dielectric dimers have also been useful for enhancing electromagnetic field hotspots [17–19]. Moreover, metasurfaces consisting of nanopillars with nanotrenches can produce spatially modulated electric field enhancements or tunable "hot spots"

#402259 https://doi.org/10.1364/OE.402259
Journal © 2020 Received 7 Jul 2020; revised 13 Sep 2020; accepted 24 Sep 2020; published 6 Oct 2020

Optics EXPRESS

[20], which can be used to improve the sensitivity and light-material interaction. High-aspect-ratio structures, which support surface plasmon resonance along the vertical direction, can be defined precisely in the fabrication steps of standard top down processes including photolithography and reactive ion etching [21]. Several types of modes are hybridized in the coupling, which can lead to narrower linewidths of the resonances [22].

Using metasurfaces to detect multiple molecules requires multiple resonances, and several methods have been reported. Chen *et al.* utilized a polarization-sensitive array of vertically coupled complementary antennas to achieve dual-mode molecule sensing in the infrared range [11]. Celebrano *et al.* described a non-axial-symmetry single-crystalline gold nanostructure to obtain double mode resonance [23]. Boriskina *et al.* embedded bow-tie nanoantennas or dimer gaps into multiple-periodic gratings to produce multiwavelength resonances in the visible range [24]. Liu *et al.* reported a triple-layer dielectric metamaterial with a metal substrate to achieve multiple absorption bands in the visible range [25].

These developments point towards the use of metasurfaces as efficient biosensors. A primary concern when using the metasurface as a biosensor is the biocompatibility of the material. Complications associated with metal surfaces and cultured cells, such as corrosion especially in the presence of biochemicals, make dielectric materials the preferred option [26,27]. Moreover, the choice of operating wavelength of the probing light should be within the optical window of biological tissues where the probing light is least invasive to the biological sample and least absorbed by water. Such optical window falls within the near infrared region [28,29]. Using a probe light within the near infrared region therefore makes it possible to sense refractive indices with less invasive effects compared to using a probe light that matches with certain absorption bands of bio-molecules. Since dielectric metasurfaces have flexibility of varying doping carriers [30], we can therefore design a dielectric-based metasurface whose resonant modes fall within the near-infrared region. Furthermore, each resonant mode should be distinct so it can be used to sense a range of refractive index gradients.

To address these issues, we propose a novel metasurface design to visualize gradients in refractive index along the sensing plane. The metasurface consists of a high-aspect-ratio dielectric array of nanopillars that produces electromagnetic field enhancements with multiple but distinct resonant modes in the near infrared region. The resonant modes can be tuned by the height and diameter of the nanopillar as well as the diameter of the nanotrench at the center of each nanopillar. Moreover, the linewidth of the resonant modes can be also be tuned using a thin metal layer sandwiched between the dielectric substrates [31]. To assess its performance, we calculated the three-dimensional (3D) electromagnetic field distribution at constant and varying refractive indices of the surrounding medium. Rather than measuring shifts in the spectra, we propose a unique sensing paradigm where we illuminate the metasurface using light set to a particular resonance. A similar approach has been proposed by Rodionov, *et al.* where they measured the gradients in refractive index by the redistribution of intensities between transmitted diffraction orders [32]. Our approach, on the other hand, works by imaging the field enhancements at the nanopillars and effectively visualizing the two-dimensional map of the spatial distribution of a range of refractive indices. Using numerical simulations, we show effective imaging of refractive index gradients along the metasurface paving the way for their use as a biosensor for complex biochemical distributions along the sensing plane.

2. Biocompatible 2D model of the metasurface sensor

We first describe a two-dimensional (2D) model to assess its fundamental optical properties by varying the diameter of the nanotrench, height and diameter of the nanopillar as well as the thickness of the metal layer. Figure 1(a) shows the proposed metasurface consisting of an array of nanopillars (diameter D, depth h and period p). Each nanopillar has a nanotrench (diameter δ) at the center. The base of the nanopillars consists of a 10-nm-thick dielectric layer and a metal

Optics EXPRESS

plane (thickness τ) on top of a glass substrate. The dielectric layer protects the metal surface from corrosion or contact with the cells and biochemicals. To assess its optical properties, a uniform transverse magnetic (TM) polarized light is incident vertically from the topside of the metasurface represented by the wave vector of k_z, and electric vector of E_x. On the other hand, light with transverse electric (TE) polarization is directed orthogonal with respect to TM along the transverse direction.

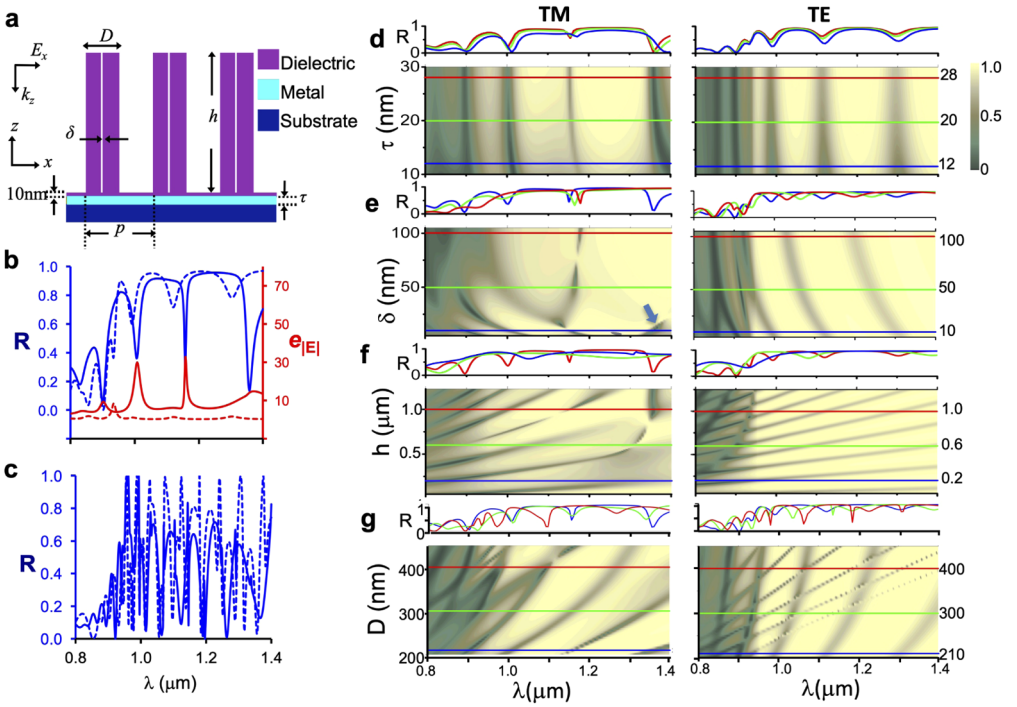

Fig. 1. 2D model.(a) Schematic of the metasurface. (b) Normalized reflectivity spectra (blue) and electric field enhancement (red) of the metasurface with a nanotrench diameter, δ = 10 nm, nanopillar height, h = 1μm and τ = 20 nm-thick metal layer using an incident TM (solid) and TE (dashed) polarized light. (c) An all-dielectric metasurface with τ = 0 yields a complex reflectivity spectrum. The reflectivity spectra with varying design parameters: (d) metal plane thickness from 10 <τ< 30 nm with constant nanotrench diameter δ = 10 nm, nanopillar height h = 1 μm and nanopillar diameter D = 200 nm; (e) nanotrench diameter from 5 <δ< 100 nm with constant h = 1 μm, D = 200 nm and τ= 20 nm; (f) nanopillar height from 0.05 <h<1.2 μm with constant δ=10 nm, τ=20 nm and D = 200 nm; and (g) nanopillar diameter from 200 <D<450 nm with constant τ=20 nm, δ = 10 nm and h = 1 μm using an incident TM (left) and TE (right) polarized light. We used a glass substrate with thickness of at least 1 μm. Color scale represents the normalized reflectivity.

We used finite element methods (COMSOL Multiphysics software package) to numerically calculate the reflectivity spectra as well as the electric field distributions. To reduce the computational complexity, we set a periodic boundary condition in the x direction and divided the calculating domain into two regions depending on the feature size. The region inside the nanopillar (which includes the nanotrench) has a minimum mesh size of 0.1 nm and maximum of 1 nm. On the other hand, the region outside the nanopillar including the base substrate has minimum mesh size of 1 nm and maximum of 20 nm. We have compared the results with those calculated with a constant mesh size all throughout and the results are comparable. Taking into account dispersion, we obtained the refractive indices of aluminium and silicon as a function of

Optics EXPRESS

wavelength from known sources [33–35]. From the electric field distribution, we calculated the electric field enhancement, $e_{|E|}$, by integrating over an area, A, around the nanopillar over their corresponding integrated incident fields, giving us $e_{|E|} = \int |E| \mathrm{d}A / \int |E_{\mathrm{in}}| \mathrm{d}A$.

Figure 1(b) shows the reflectivity spectra (blue) and corresponding electric field enhancement (red) using normal incidence of a TM (solid) and TE (dashed) polarized light with wavelength varied from 0.8 μm to 1.4 μm. The resonances occur in the near infrared with TM polarization exhibiting better contrast at resonance. On the other hand, the maximum value of the $e_{|E|}$ with TM polarized light is about seven times stronger than that with TE polarized light. The strong field enhancement is due to our nanopillar design with nanotrench that supports bonding and antibonding modes that are strongly localized on the gap domain [17,36,37]. Both the reflectivity and field enhancements decrease at wavelengths shorter than the infrared and optimum at longer wavelengths. As such, our system has lesser potential for its application using visible probe light.

We assessed the effect of the metal plane by calculating the reflectivity spectra for a similar structure in the absence of the metal plane or by setting $\tau = 0$. The reflectivity spectra with TM and TE polarized light have multiple and closely spaced resonant modes with narrower linewidths, as shown in Fig. 1(c). While resonant modes with narrow linewidths may be beneficial for certain biosensor mechanisms, its potential use for our sensing paradigm will produce ambiguous readings especially since the modes are closely packed and cannot be differentiated. To further assess the impact of τ, we calculated the reflectivity spectra for $10 < \tau < 30$ nm. Using a TM polarized light resulted in narrower and slightly blue-shifted resonant modes with increasing τ (Fig. 1(d)-left). However, for TE polarized light (Fig. 1(d)-right), the resonant modes remain constant but with a broader linewidths as compared to that with TM polarized light.

We then investigated how the resonances are influenced by the geometry by calculating the reflectivity spectra with varying δ. Figure 1(e) shows how the reflectivity spectrum is influenced by the diameter ($5<\delta<105$nm) of the nanotrench using an incident light with TM and TE polarization. For TM polarization, majority of the resonant modes are blue-shifted with increasing diameter δ, while one mode (indicated with a blue arrow) is red-shifted. Since the periodicity of the nanopillar array and the wall thickness of the nanopillar are kept constant, increasing δ means increasing the gap size of the dimer nanoantenna, and therefore leads to higher resonance energy or blue-shifted resonance modes [38,39]. Moreover, the red-shifted resonance mode (blue arrow) is due to the narrow gap size (<20 nm) far shorter than the wavelength of a probe light, which leads to hybridization of the bonding mode and lattice mode [37]. On the other hand, an incident light with TE polarization, the resonant modes are generally blue-shifted with increasing δ.

The height and diameter of the nanopillar can set the wavelength of the resonance modes. Figure 1(f) shows how the reflectivity is influenced when the height (h) of the nanopillar is varied from $0.05<h<1.2$ μm. We found that the resonant modes are generally red-shifted with increasing h for either TM or TE polarizations. On the other hand, Fig. 1(g) shows the reflectivity spectra as the diameter of the nanopillar is increased from 200 nm to 450 nm. Similarly, the resonant modes are red shifted for either polarization states. A larger diameter or a longer height results in a longer resonant wavelength, which can be explained by the resonant waveguide model [37]. For TE polarization, the splitting of the resonant modes is potentially due to the antibonding mode excited by the incident light [37].

In this section, we have shown that the linewidth of the resonance can be tuned by the thickness of the metal plane, while the resonance wavelength can be tuned by the diameter of the nanotrench or the height and diameter of the nanopillar. For sensing refractive indices, we can optimize the structure with appropriate resonance modes with suitable contrast and bandwidth to improve the sensitivity [31]. By tailoring the structure of the nanopillar, we can identify an operating wavelength of a probing light where it matches to a certain resonant mode, which produces field

Optics EXPRESS

enhancements that are correlated with the refractive index of the surrounding medium. The resonant mode should also be broad enough so a range of refractive indices can be measured.

3. 3D model and biosensing of refractive index gradients

To assess how our metasurface can function as a biosensor, we extended our 2D model to 3D and calculated the reflectivity spectra in varying refractive indices of the surrounding medium. Figure 2(a) shows the 3D diagram of the metasurface with similar parameters as the 2D structure shown in Fig. 1(a). To simulate sensing of refractive indices, we replaced the surrounding medium from air (n = 1.0) to water (n_o = 1.33). Water in liquid form is distributed along the metasurface thereby covering all areas where air would have been present. We have not incorporated the effect of surface tension in our simulations. The reflectivity spectra of the metasurface in air and water show resonances in the near infrared (Fig. 2(b)). The shifting of the resonances to longer wavelengths is due to the coupling condition of the incident light and the nanopillar, which is highly dependent on the refractive index of the surrounding medium [13,31]. The reflectivity spectrum of the 3D structure in air is blue-shifted and compressed compared to that of the 2D model (Fig. 1(b)), but nonetheless exhibit similar features. We then systematically changed the refractive indices in the medium surrounding the metasurface and Fig. 2(c) shows linear shifts the resonances (λ_1 = 1.045μm and λ_2 = 1.108μm) towards longer wavelength (Fig. 2(d)).

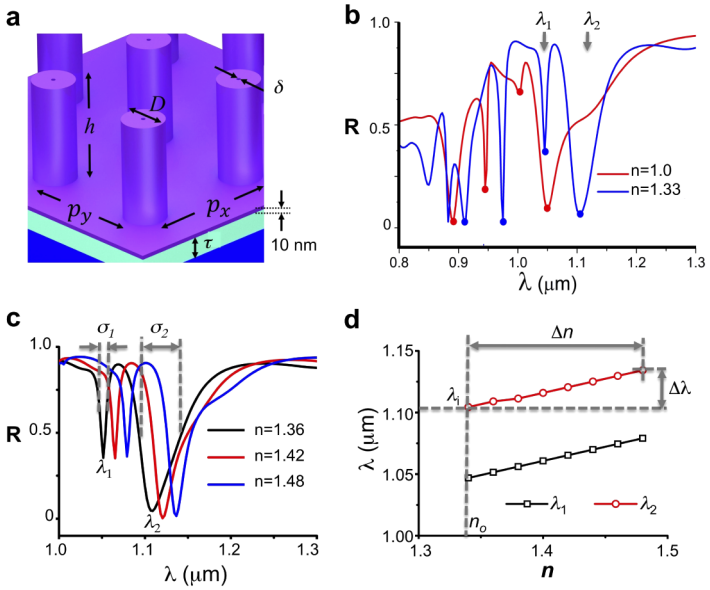

Fig. 2. 3D model. (a) Schematic of the metasurface with parameters and color scheme similar to the 2D model. (b) The reflectivity spectra of the metasurface in air and water using an incident TM polarized light. The resonance modes are generally red-shifted when the surrounding medium is changed from air (n = 1) to water (n_o = 1.33). (c) Reflectivity spectra using an incident TM polarization showing two resonance modes, λ_1 and λ_2. (d) Resonant wavelength shift for the two resonance modes with uniform refractive index of the surrounding medium varied from 1.33 to 1.48.

When using the metasurface as a biosensor, the refractive index of the surrounding medium varies with the distribution of biomolecules. Such spatial biomolecular distributions occur when the metasurface is used as an artificial niche where cells are grown [10], or when the analyte is composed of spatial clusters of bacteria or viruses. To model such operation, we used a 3×3 nanopillar array with D = 210 nm, δ = 10 nm and h = 1.0 μm and varied the refractive

Optics EXPRESS

index linearly from $1.33 \leq n \leq 1.48$ along the x-axis. To visualize the gradient in refractive index along the metasurface, we apply our unique sensing paradigm where we illuminate the metasurface using light set to a particular resonance. From the reflectivity plot in Fig. 3(c), we identified an operating wavelength to be able to translate the gradient in refractive index as a measurable quantity in terms of field enhancement. Illuminating the metasurface using light with $\lambda = \lambda_2$ sets up resonance and low reflectivity at $n = 1.36$ and consequently exhibiting high field enhancements at the nanopillars. On the other hand, the same light does not trigger resonance at $n = 1.48$ and thereby exhibiting lower field enhancements.

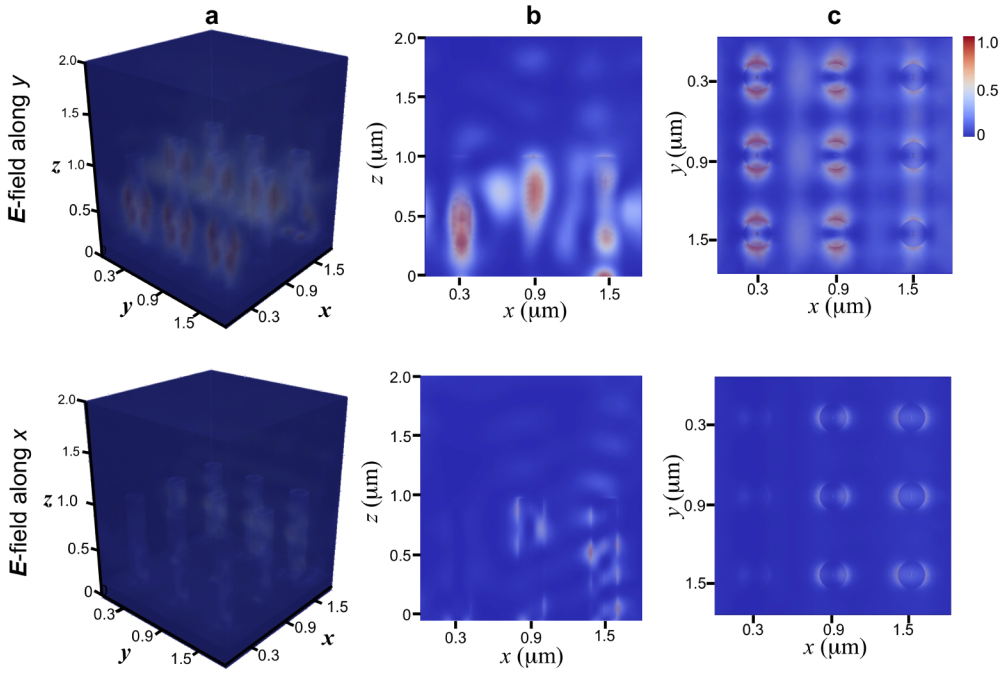

Fig. 3. Biosensing performance of the metasurface biosensor. (a) 3D intensity distribution with refractive index, n, linearly varied along the x-axis and illuminated with laser with $\lambda = \lambda_2$ and with TM polarization with E-field directed along y-axis (top row) and x-axis (bottom row). Corresponding planar (b) $xz-$ and (c) $xy-$ intensity distributions derived by integrating the intensity along the y- and z-axis, respectively. Color scale shows normalized intensity.

Figures 3(a) (top and bottom) show the 3D intensity distributions using TM polarized light with E-field along $y-$ and $x-$ directions, respectively. The corresponding intensity distributions along the xz- and xy- planes are shown in Figs. 3(b) and (c), respectively. When the E-field is directed orthogonal to the gradient in refractive index (Fig. 3 top row), the field enhancements are observed similar to resonance conditions and inversely correlated with the gradient in refractive index along the x-axis. However, when the gradient in n is along the direction of the E-field (Fig. 3 bottom row), the intensity is weaker but the enhancements yielded a positive correlation with varying n. Such polarization dependence sensing can produce a full 2D map of arbitrary refractive index gradients by acquiring and integrating two intensity distributions using both TM polarized light with E-fields rotated along the x and y directions. Planar observation of the intensity distribution along xy plane can therefore be used to sense changes in refractive index, which can be correlated with the biochemical gradients along the metasurface.

Optics EXPRESS

4. Discussion

For biosensing applications, metasurfaces can be used as scaffolds [10], electrical probes [40] and Raman analysis [20,41] for probing growth and function of cells. The sensitivity of the biosensor to the refractive index of the surrounding medium is one of the key features we used for sensing [42]. To obtain a biosensor with high sensitivity, we selected a resonant mode with a large modulation depth. We can evaluate the sensing performance by calculating the sensitivity using the ratio between resonant wavelength shift ($\Delta\lambda$) and change of the refractive index (Δn) of the surrounding medium, given by $S = \Delta\lambda/\Delta n$ (nm) (Fig. 2(d)). Inversely, the refractive index of the surrounding medium can be acquired from S using the relation $n = n_o + (\lambda_i' - \lambda_i)/S$, where λ_i' is the resonant position shifted from λ_i (Fig. 2(d)). We identify a dimensionless sensing range, Δn_{max}, which takes the ratio of the full-width at half maximum (σ) and sensitivity for a specific resonance, giving us $\Delta n_{max} = \sigma/S$. For λ_1, we calculated $S = 226.7$ nm, $\sigma_1 = 8.9$ nm and $\Delta n_{max} = 0.039$. On the other hand, for λ_2, we calculated $S = 193.3$ nm, $\sigma_2 = 48.5$ nm and $\Delta n_{max} = 0.251$ (see Fig. 2(c)). In other sensing paradigms, the figure of merit, $FoM = \Delta n_{max}^{-1}$, is often used to assess the sharpness of the resonance [8]. However, within our sensing paradigm, Δn_{max} defines the maximum Δn (with respect to n_o) that can be detected by our biosensor. This implies that a narrow σ provides for a highly resolved sensor but with a limited range in detecting refractive index gradients. On the other hand, a sensor with lesser resolution but with larger coverage in Δn is provided by a broad σ.

5. Conclusion

From a theoretical framework, we have proposed a novel sensing paradigm capable of sensing gradients in refractive index of the medium surrounding the metasurface. The variations in refractive index are highly correlated with the field enhancements at the nanopillars. The operating conditions can be tuned to available light sources by tailoring the geometry of the metasurface (δ, h, D and τ). Due to the varying bandwidths of certain resonant modes, our metasurface can well be applied as a refractive index sensor with different sensitivities. A narrow bandwidth provides for higher resolution but with limited range in Δn. Other resonance positions can also be used depending on the estimated range of n and sensitivity. This theoretical framework paves the way for sensing of biochemical distributions and potentially their concentrations after performing the necessary calibrations with fabricated metasurfaces. The applicability of our metasurface-based biosensor and our novel sensing paradigm extends to lab-on-a-chip sensors requiring fast imaging and assessment of portable testing kits for biochemical, bacteria or virus distributions.

Funding

China Scholarship Council (201708410455); Science and Technology Department of Henan Province (182102210122); Xinxiang Medical University (505212); National Health and Medical Research Council (PG1105944); Australian Research Council (DE180100775).

Acknowledgments

We thank Prof. Chennupati Jagadish for the advise and comments on the manuscript. This work was undertaken with the assistance of resources from the National Computational Infrastructure, which is supported by the Australian Government. The data that support the findings of this study are available from the corresponding authors upon reasonable request.

Disclosures

The authors declare no conflicts of interest.

Optics EXPRESS

References

1. A. Tittl, A. Leitis, M. Liu, F. Yesilkoy, D.-Y. Choi, D. N. Neshev, Y. S. Kivshar, and H. Altug, "Imaging-based molecular barcoding with pixelated dielectric metasurfaces," Science **360**(6393), 1105–1109 (2018).
2. M. Holgado, C. Barrios, F. Ortega, F. Sanza, R. Casquel, M. Laguna, M. Ba nuls, D. López-Romero, R. Puchades, and A. Maquieira, "Label-free biosensing by means of periodic lattices of high aspect ratio su-8 nano-pillars," Biosens. Bioelectron. **25**(12), 2553–2558 (2010).
3. Y. Lee, S.-J. Kim, H. Park, and B. Lee, "Metamaterials and metasurfaces for sensor applications," Sensors **17**(8), 1726 (2017).
4. Y. Peng, C. Shi, Y. Zhu, M. Gu, and S. Zhuang, "Terahertz spectroscopy in biomedical field: a review on signal-to-noise ratio improvement," PhotoniX **1**(1), 12–18 (2020).
5. Q. Ma, Q. R. Hong, X. X. Gao, H. B. Jing, C. Liu, G. D. Bai, Q. Cheng, and T. J. Cui, "Smart sensing metasurface with self-defined functions in dual polarizations," Nanophotonics **9**(10), 3271–3278 (2020).
6. Z. Li, E. Palacios, S. Butun, H. Kocer, and K. Aydin, "Omnidirectional, broadband light absorption using large-area, ultrathin lossy metallic film coatings," Sci. Rep. **5**(1), 15137 (2015).
7. J. Park, J. Kang, X. Liu, S. J. Maddox, K. Tang, P. C. McIntyre, S. R. Bank, and M. L. Brongersma, "Dynamic thermal emission control with inas-based plasmonic metasurfaces," Sci. Adv. **4**(12), eaat3163 (2018).
8. N. Liu, M. Mesch, T. Weiss, M. Hentschel, and H. Giessen, "Infrared perfect absorber and its application as plasmonic sensor," Nano Lett. **10**(7), 2342–2348 (2010).
9. B. D. Choudhury, R. Casquel, M. Ba nuls, F. Sanza, M. Laguna, M. Holgado, R. Puchades, A. Maquieira, C. Barrios, and S. Anand, "Silicon nanopillar arrays with sio 2 overlayer for biosensing application," Opt. Mater. Express **4**(7), 1345–1354 (2014).
10. V. Gautam, S. Naureen, N. Shahid, Q. Gao, Y. Wang, D. Nisbet, C. Jagadish, and V. R. Daria, "Engineering highly interconnected neuronal networks on nanowire scaffolds," Nano Lett. **17**(6), 3369–3375 (2017).
11. X. Chen, C. Wang, Y. Yao, and C. Wang, "Plasmonic vertically coupled complementary antennas for dual-mode infrared molecule sensing," ACS Nano **11**(8), 8034–8046 (2017).
12. A. Cetin, A. A. Yanik, C. Yilmaz, S. Somu, A. Busnaina, and H. Altug, "Monopole antenna arrays for optical trapping, spectroscopy, and sensing," Appl. Phys. Lett. **98**(11), 111110 (2011).
13. X. Lu and J. Lin, "Field enhancement of a metal grating with nanocavities and its sensing applications," J. Opt. **19**(5), 055004 (2017).
14. A. E. Cetin, A. A. Yanik, C. Yilmaz, S. Somu, A. Busnaina, and H. Altug, "Plasmonic nanopillar arrays for optical trapping, biosensing, and spectroscopy," Proc. SPIE **8097**, 80971P (2011).
15. I. Staude and J. Schilling, "Metamaterial-inspired silicon nanophotonics," Nat. Photonics **11**(5), 274–284 (2017).
16. O. Yavas, M. Svedendahl, P. Dobosz, V. Sanz, and R. Quidant, "On-a-chip biosensing based on all-dielectric nanoresonators," Nano Lett. **17**(7), 4421–4426 (2017).
17. F. Zhang, V. Sadaune, L. Kang, Q. Zhao, J. Zhou, and D. Lippens, "Coupling effect for dielectric metamaterial dimer," Prog. Electromagn. Res. **132**, 587–601 (2012).
18. R. M. Bakker, D. Permyakov, Y. Yu, D. Markovich, R. Paniagua-Domínguez, L. Gonzaga, A. Samusev, Y. Kivshar, B. Luk'yanchuk, and A. I. Kuznetsov, "Magnetic and electric hotspots with silicon nanodimers," Nano Lett. **15**(3), 2137–2142 (2015).
19. F. Ding, Y. Yang, R. A. Deshpande, and S. I. Bozhevolnyi, "A review of gap-surface plasmon metasurfaces: fundamentals and applications," Nanophotonics **7**(6), 1129–1156 (2018).
20. J. Huang, Y. Zhao, X. Zhu, and W. Zhang, "Averaging effect on improving signal reproducibility of gap-based and gap-free sers substrates based on ordered si nanowire arrays," RSC Adv. **7**(9), 5297–5305 (2017).
21. T. Ozel, B. A. Zhang, R. Gao, R. W. Day, C. M. Lieber, and D. G. Nocera, "Electrochemical deposition of conformal and functional layers on high aspect ratio silicon micro/nanowires," Nano Lett. **17**(7), 4502–4507 (2017).
22. A. Kabashin, P. R. Evans, S. Pastkovsky, W. Hendren, G. A. Wurtz, R. Atkinson, R. Pollard, V. A. Podolskiy, and A. V. Zayats, "Plasmonic nanorod metamaterials for biosensing," Nat. Mater. **8**(11), 867–871 (2009).
23. M. Celebrano, X. Wu, M. Baselli, S. Großmann, P. Biagioni, A. Locatelli, C. De Angelis, G. Cerullo, R. Osellame, B. Hecht, L. Duo, F. Ciccaci, and M. Finazzi, "Mode matching in multiresonant plasmonic nanoantennas for enhanced second harmonic generation," Nat. Nanotechnol. **10**(5), 412–417 (2015).
24. S. V. Boriskina and L. Dal Negro, "Multiple-wavelength plasmonic nanoantennas," Opt. Lett. **35**(4), 538–540 (2010).
25. Z. Liu, G. Liu, G. Fu, X. Liu, and Y. Wang, "Multi-band light perfect absorption by a metal layer-coupled dielectric metamaterial," Opt. Express **24**(5), 5020–5025 (2016).
26. S. Hiromoto, "Corrosion of metallic biomaterials in cell culture environments," The Electrochemical Society Interface **17**(2), 41 (2008).
27. D. F. Williams, "On the mechanisms of biocompatibility," Biomaterials **29**(20), 2941–2953 (2008).
28. A. Smith, M. Mancini, and S. Nie, "Second window for in vivo imaging," Nat. Nanotechnol. **4**(11), 710–711 (2009).
29. A. Alabugin, "Near-ir photochemistry for biology: Exploiting the optical window of tissue," Photochem. Photobiol. **95**(3), 722–732 (2019).
30. S. Jahani and Z. Jacob, "All-dielectric metamaterials," Nat. Nanotechnol. **11**(1), 23–36 (2016).
31. X. Lu, T. Zhang, R. Wan, Y. Xu, C. Zhao, and S. Guo, "Numerical investigation of narrowband infrared absorber and sensor based on dielectric-metal metasurface," Opt. Express **26**(8), 10179–10187 (2018).

Optics EXPRESS

32. S. A. Rodionov, M. A. Remnev, and V. V. Klimov, "Refractive index sensor based on all-dielectric gradient metasurface," Sens. Bio-sensing Res. **22**, 100263 (2019).
33. K. M. McPeak, S. V. Jayanti, S. J. P. Kress, S. Meyer, S. Iotti, A. Rossinelli, and D. J. Norris, "Plasmonic films can easily be better: rules and recipes," ACS Photonics **2**(3), 326–333 (2015).
34. D. T. Pierce and W. E. Spicer, "Electronic structure of amorphous si from photoemission and optical studies," Phys. Rev. B **5**(8), 3017–3029 (1972).
35. E. D. Palik, *Handbook of optical constants of solids*, vol. 3 (Academic, 1998).
36. S. Zhang, K. Bao, N. J. Halas, H. Xu, and P. Nordlander, "Substrate-induced fano resonances of a plasmonic nanocube: a route to increased-sensitivity localized surface plasmon resonance sensors revealed," Nano Lett. **11**(4), 1657–1663 (2011).
37. S. Zhang and H. Xu, "Tunable dark plasmons in a metallic nanocube dimer: toward ultimate sensitivity nanoplasmonic sensors," Nanoscale **8**(28), 13722–13729 (2016).
38. M. Kaniber, K. Schraml, A. Regler, J. Bartl, G. Glashagen, F. Flassig, J. Wierzbowski, and J. Finley, "Surface plasmon resonance spectroscopy of single bowtie nano-antennas using a differential reflectivity method," Sci. Rep. **6**(1), 23203 (2016).
39. K. Schraml, M. Spiegl, M. Kammerlocher, G. Bracher, J. Bartl, T. Campbell, J. Finley, and M. Kaniber, "Optical properties and interparticle coupling of plasmonic bowtie nanoantennas on a semiconducting substrate," Phys. Rev. B **90**(3), 035435 (2014).
40. M. Dipalo, H. Amin, L. Lovato, F. Moia, V. Caprettini, G. C. Messina, F. Tantussi, L. Berdondini, and F. De Angelis, "Intracellular and extracellular recording of spontaneous action potentials in mammalian neurons and cardiac cells with 3d plasmonic nanoelectrodes," Nano Lett. **17**(6), 3932–3939 (2017).
41. J. Huang, Y. Zhao, X. Zhang, L. He, T. Wong, Y. Chui, W. Zhang, and S. Lee, "Ordered ag/si nanowires array: wide-range surface-enhanced raman spectroscopy for reproducible biomolecule detection," Nano Lett. **13**(11), 5039–5045 (2013).
42. J. Zhao, X. Zhang, C. R. Yonzon, A. J. Haes, and R. P. Van Duyne, "Localized surface plasmon resonance biosensors," Nanomedicine **1**(2), 219–228 (2006).